NIR-responsive carbon dots as an oxidative-stress amplifier and hyperthermia-induced superior photothermal *in-vitro* anticancer activity

Md Moniruzzaman [a,1], Sayan Deb Dutta [b,c,d,1], Rumi Acharya [b,e], Ki-Taek Lim [b,c,e,*,2], Jongsung Kim [a,**,3]

[a] *Department of Chemical and Biological Engineering, Gachon University, 1342 Seongnam-daero, Seongnam-si, Gyeonggi-do 13120, Republic of Korea*
[b] *Department of Biosystems Engineering, Kangwon National University, Chuncheon, Gangwon-do 24341, the Republic of Korea*
[c] *Institute of Forest Science, Kangwon National University, Chuncheon, Gangwon-do 24341, the Republic of Korea*
[d] *Center for Surgical Bioengineering, School of Medicine, University of California Davis, Sacramento 95817, United States*
[e] *Interdisciplinary Program in Smart Agriculture, Kangwon National University, Chuncheon, Gangwon-do 24341, the Republic of Korea*

HIGHLIGHTS

- Polyphenolic CDs with extended π-conjugation and orange emission were prepared.
- Hydrophilic O-CDs showed good NIR-harvesting potential with excellent PCE~58%.
- Apoptosis-related proteins and genes were upregulated due to the photothermal effect
- NIR-induced oxidative-stress in cooperation with hyperthermia, kills cancer cells.

GRAPHICAL ABSTRACT
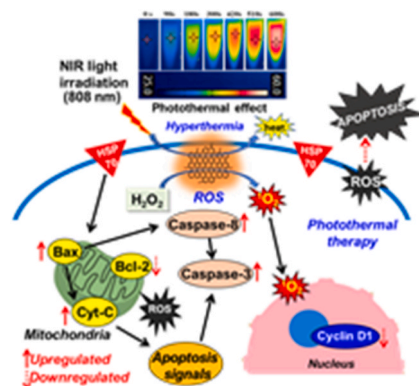
ARTICLE INFO

ABSTRACT

A facile wet chemistry-based strategy was developed to synthesize orange emissive Carbon dots (O-CDs) based on dehydration-induced ring-fusion of the precursor (1,3-dihydroxynaphthalene) in a dehydrating sulfuric acid medium. The O-CDs revealed significant Near-infrared (808 nm) light harvesting potential with outstanding photothermal conversion efficiency (~58%) and hence exhibited excellent NIR-light stimulated photothermal anticancer performance. Furthermore, these fluorescent O-CD nanoprobes displayed excitation-dependent polychromatic emissions in the range of 540–640 nm, with the dual emission maxima at 540 and 580 nm, corresponding to yellow and orange emission at the excitation of 490 nm. Various mitochondrial, as well as

* Corresponding author at: Department of Biosystems Engineering, Kangwon National University, Chuncheon, Gangwon-do 24341, the Republic of Korea.
** Corresponding author.
E-mail addresses: ktlim@kangwon.ac.kr (K.-T. Lim), jongkim@gachon.ac.kr (J. Kim).
[1] These authors contributed equally to this manuscript.
[2] orcid.org/0000-0003-2091-788X
[3] orcid.org/0000-0001-8885-0533

cytoplasmic apoptosis-related proteins and genes were upregulated during photothermal treatment, which suggests that hyperthermia and oxidative stress have a major impact on cell death. The anticancer activity of O-CDs is likely due to the elevated reactive oxygen species (ROS) amplification in cooperation with the hyperthermia effect. This study offers a potential alternative to bio-nanomedicine for cancer treatment by carbon-based photothermal therapy.

1. Introduction

Near-infrared radiation (NIR) responsive photothermal agents (PTAs) have emerged as an outstanding substitute for chemotherapeutic drugs because of their low side effects, minimal invasiveness, and high specificity toward tumors [1,2]. PTAs exploit photon energy and transform it into heat, resulting in local hyperthermia, which combats infectious cancer cells[3]. A number of PTAs, such as metallic oxides, metal chalcogenides, noble metal-based nanomaterials, organic NIR-chromophores, and polymeric nanocomposites, have been widely explored for NIR-mediated photothermal action to destroy cancerous cells [4–9]. However, conventional PTAs possess high toxicity and lower photothermal conversion efficiency (PCE), which limits their therapeutic application [10,11]. In contrast, carbon-based nanoparticles have drawn remarkable appreciation because of their favorable physiochemical properties, low cytotoxicity, and comparatively higher biosafety [12–15].

carbon dots (CDs) with distinct photoluminescent characteristics have fascinated researchers because of their broad range of applications, which include sensing, bioimaging, photocatalysis, drug delivery, and wound healing [16–24]. Recent advances in the usage of CDs as superior photoactive materials for photothermal therapy are notable [25]. More importantly, CDs have been well explored as excellent photoactive and NIR-responsive agents for photothermal therapeutic application in cancer or bacterial disease. For instance, Jia et al. produced Hypocrella bambusae-derived CDs, which could be used as NIR-responsive (635 nm) photothermal therapeutic agents for cancer treatment [26]. Ge et al. synthesized polythiophene phenylpropionic acid-derived CDs with red emission having NIR-responsive behavior under 671 nm laser as superior photothermal nanotheranostic agents for cancer diagnosis and cure [27]. Nevertheless, their usage in clinical practice is constrained by the application of high-frequency radiation that has inadequate tissue permeation and low PCE. Furthermore, a few investigations have been attempted utilizing long-wavelength NIR lasers; however, they exhibited insufficient PCE. For instance, Li et al. synthesized watermelon-derived CDs with NIR-II emission and good NIR-harvesting (808 nm) properties but exhibited photothermal PCE reaching only 30.6% [28]. Therefore, it is essential to design suitable CD-based NIR-light-sensitive biocompatible PTAs with high PCE.

According to prior studies, enhancing the extent of conjugation degree into the carbon framework may significantly boost the light-harvesting ability for longer wavelengths, which is beneficial for obtaining high PCE. Several attempts have been undertaken to produce CD nanostructures with extended π-conjugation via meticulously screening proper polycyclic aromatic precursors for NIR-responsive photothermal treatment. For instance, pyrene and coronene were previously investigated as aromatic hydrocarbon precursors to produce CDs with extended π-conjugation exhibiting superior NIR-harvesting characteristics and good PCE for photothermal tumor therapy [3,29,30]. Similarly, Perylene and polythiophene have also been explored to develop extended π-conjugated CDs nanostructure with superior NIR-harvesting features and good PCE for photothermal bactericidal and anticancer properties [31,32]. Consequently, it is of utmost interest for the current researchers to explore a variety of suitable polycyclic aromatic precursors to manufacture CDs with extended π-conjugation and superior NIR-triggered photothermal properties for diverse applications.

Herein, we adopted a wet-chemistry-based synthesis approach to produce orange emissive polyphenolic-CDs based on dehydration-induced ring-fusion involving six-membered ring cyclization of the precursor (1,3-dihydroxynaphthalene) in dehydrating sulfuric acid medium. The as-synthesized O-CDs demonstrated superior NIR-light (808 nm) harvesting properties with impressive PCE ~58% and revealed excellent NIR-triggered photothermal combat of infectious cancerous cells. Various mitochondrial as well as cytoplasmic apoptosis-related proteins and genes were upregulated during photothermal treatment, which suggests that hyperthermia and oxidative stress have a major impact on cell death.

2. Experimental

2.1. Synthesis of O-CDs

In a typical synthesis procedure, 1,3-dihydroxy naphthalene (200 mg) was added to a 100 mL glass beaker containing 5 mL each of water and ethanol, followed by the addition of 2 mL concentrated H_2SO_4. The solution was then kept in a hot air oven preheated to a constant temperature of 190 °C, and the reaction time was maintained for 100 min. After the thermal reaction, the beaker was immediately taken out and cooled naturally to room temperature. After adding 15 mL of DI water, centrifugation was performed at high speed (10 000 rpm) to collect the desired CQDs, which were washed with water once followed by dialysis (using cellulose ester membrane with a molecular weight cut-off of 500 Da) for 24 h against DI water. The dialyzed product was centrifuged at 4000 rpm to discard any agglomerated particles and finally dried to obtain a black O-CDs powder, as shown in **Figure S1 (electronic supplementary information, ESI†)**. The as-synthesized O-CDs are well dispersible in water and stable as shown in **Figure S1c (ESI†).**

2.2. Photothermal experiment and PCE Measurement of O-CDs

For *in vitro* photothermal measurements, the O-CDs (200, 300, and 400 μg mL^{-1}) were placed in a 1.5 mL Eppendorf tube and irradiated with an 808-nm NIR-laser for 10 min. The temperature change was recorded using a NIR camera (FLIR-E6390, FLIR, Sweden). The PCE was evaluated by monitoring the temperature variation of aqueous O-CDs solution (DI water, neutral pH, 300 μg/mL) as a function of time while exposed to constant irradiation of NIR-radiation (808 nm, 1 W/cm^2, 10 min). DI water was taken as a negative control. A digital infrared thermal camera was used to record and image the solution temperature variation during the experiment. The PCE has been calculated employing Eq. (1), which has been mentioned in earlier papers [3,27,33,34].

$$\eta = \frac{hA(T_{max} - T_{surr}) - Q_{Dis}}{I(1 - 10^{-A\lambda})} \tag{1}$$

where **A** and **h** refer to the container's surface area and heat transfer coefficient, respectively. **T$_{surr}$** and **T$_{max}$** indicate the surrounding's temperature (26.5 °C) and equilibrium temperature (56.8 °C), respectively. Q$_{Dis}$ denotes the heat dissipated by the solvent during light absorption. ***I*** signify the incident laser power, and **Aλ** denotes the absorbance of O-CDs at 808 nm. ***hA*** was calculated using Eq. (2):

$$\tau_S = \frac{m_D c_D}{hA} \tag{2}$$

where τ$_S$ denotes the time constant determined from the cooling profile. m$_D$ and c$_D$ represent the mass (1 g) and heat capacity (4.18 J/g) of the

experimental solvent (DI water), respectively. To assess τ_S, θ should be considered using Eq. (3):

$$\theta = \frac{\Delta T}{\Delta T_{max}} \qquad (3)$$

where ΔT indicates temperature variation between system solution temperature and room temperature, while ΔT_{max} denotes temperature variation at the maximum steady-state temperature.

The value of τ was obtained from the linear plot of cooling time vs -ln (θ) according to Eq. (4)

$$t = -\tau(\ln\theta) \qquad (4)$$

The value of **hA** was estimated to be 0.008. Thus, the PCE (η) of the O-CDs solution was measured to be ~58%.

3. Results and discussion

3.1. Formation mechanism, structure, and surface properties of O-CDs

1,3-dihydroxynaphthalene, a polycyclic aromatic phenolic compound, was strategically selected as a carbon precursor to design CDs

with the π-conjugated core. Previous findings on the synthesis of phloroglucinol and naphthoresorcinol-derived CDs served as inspiration for the polyphenolic O-CDs synthesis [35–37]. A number of 1,3-dihydroxynaphthalene monomers encountered six-membered ring cyclization by trimolecular reaction pathway in the presence of dehydrating H_2SO_4, resulting in the formation of orange emissive polyaromatic π-conjugated structure as shown in the Fig. 1a [35,36]. The morphology of the as-synthesized particles was measured using high-resolution transmission electron microscopy (HR-TEM). As shown in Fig. 1b, the HR-TEM image of O-CDs displayed an average particle size of 3–7 nm with a well-ordered lattice spacing of 0.21 nm, revealing an interplanar distance of (100) plane, indicating a defect-free graphene structure [35]. The particle size distribution plot has been shown in **Figure S2a (ESI†)**. The microstructure and phase composition of the nanostructured CDs were studied using X-ray diffraction (XRD) spectroscopy. The XRD spectra (Fig. 1c) of precursor (1,3-dihydroxynaphthalene) demonstrated multiple sharp crystalline peaks at ~ 11.2°, ~16.5°, ~19.5°, ~22.5°, ~25.6°, ~28.2°, ~33.9°, ~36.3°, and ~44.2°, which was transformed into a distinctive broad peak at 2θ ~ 24.7°, corresponding to (001) lattice of graphitic carbon [16,36]. The Raman spectra were acquired to analyze the fundamental structure of O-CDs, as shown in Fig. 1d. Raman
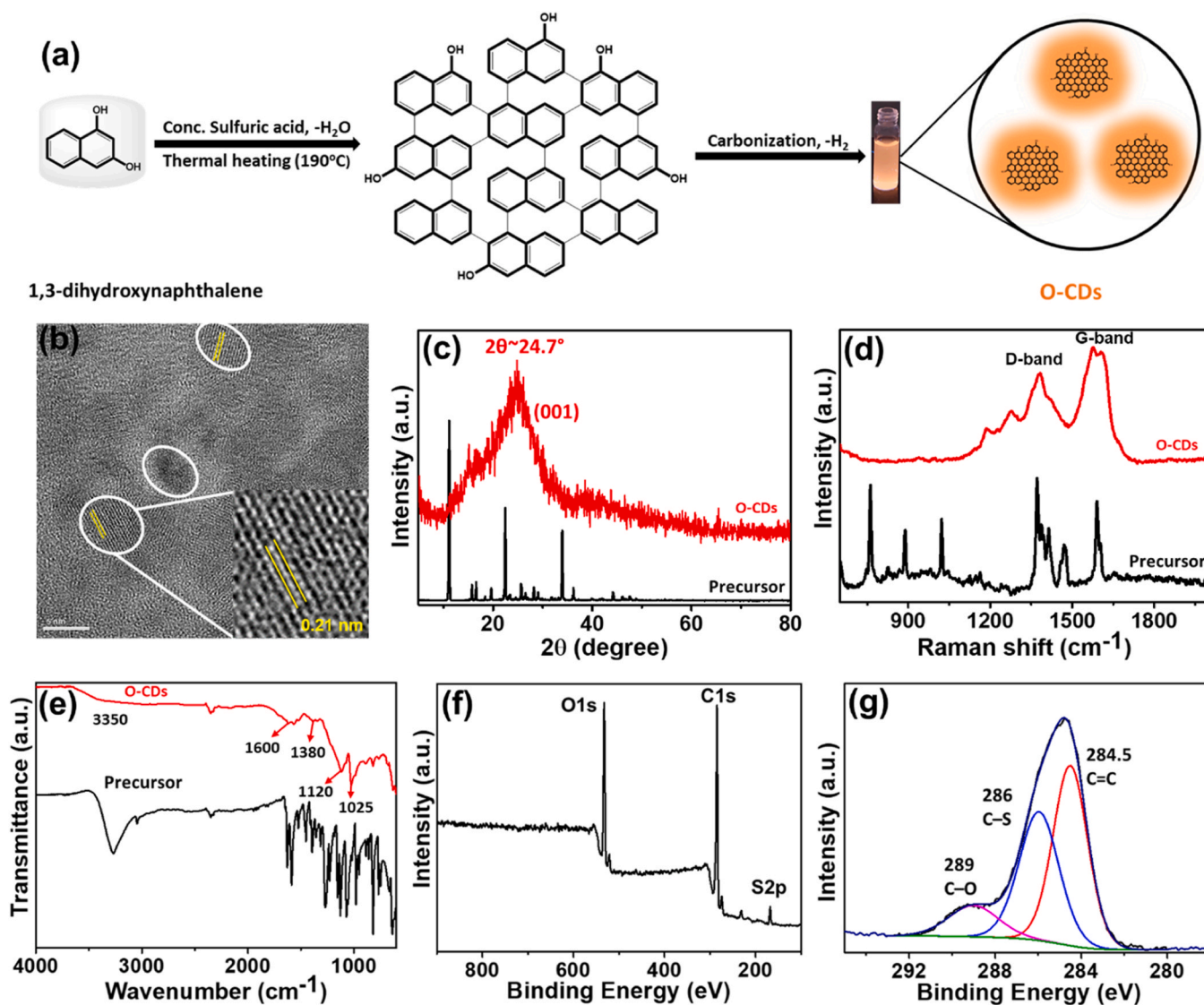

Fig. 1. (a) Schematic for the formation of O-CDs; (b) HR-TEM image (inset is the magnified portion of particle showing lattice spacing; (c) powder XRD spectra of precursor (black line) and O-CDs (red line); (d) Raman spectra of precursor (black line) and O-CDs (red line); (e) FT-IR spectra of precursor (black line) and O-CDs (red line); (e) XPS total survey spectra of PY-CDs (red line), and nitroperylene (black line); (f) XPS total survey spectra of O-CDs; (g) deconvoluted XPS spectra of C1s.

spectra of precursor (1,3-dihydroxynaphthalene) exhibited numerous unknown peaks, while O-CDs revealed characteristic peaks indicating a significant degree of graphitization. O-CDs showed typical bands at ~1380 and ~1590 cm^{-1}, representing D-and G-band, respectively [17]. The D-band at 1380 cm^{-1} indicates the existence of disordered sp^3 hybridized carbons in the structure. The G-band at 1590 cm^{-1} suggests the existence of sp^2 hybridized carbon in the framework, indicating a substantial degree of graphitization [20]. An I_G/I_D ratio (G band intensity: D band intensity) greater than unity corresponds to high-quality graphene-structured CDs. These results imply the formation of O-CDs with large and extended π-conjugated polyaromatic networks. The surface functional moieties were assessed using Fourier-transform infrared (FT-IR) spectroscopy as shown in Fig. 1e. The FT-IR spectra of O-CDs displayed the characteristic stretching vibrations of O–H and C–O/C–S chemical bonds at 3350 and 1120 cm^{-1}, respectively [17]. The FT-IR peak at 1600 cm^{-1} is due to the C═C stretching vibration of the polycyclic carbon framework with phenolic hydroxyl groups at the edges [38,39]. The two emerging peaks at nearly 1380 and 1025 cm^{-1} are the stretching vibrations of sulfonyl groups (–SO$_3$H) [40]. Thus, the FTIR spectra reveal that the CDs were composed of C–S, C–O, C═C, and C–SO$_3$H chemical bonds. XPS spectra were analyzed to survey the elemental valence states and chemical composition of the samples. As shown in Fig. 1f, the XPS total survey profile exhibited three peaks due to O 1 s, C 1 s, and S 2p, which indicate that the O-CDs are primarily composed of three elements (O, C, and S). The deconvoluted C 1 s spectra (Fig. 1g) showed three peaks at 289, 286, and 284.5 eV, signifying the existence of C–O, C–S, and C═C chemical bonds, respectively [41]. Moreover, the deconvoluted S 2p spectrum (**Figure S2b**) exhibited a peak at 168.3 eV, suggesting the presence of surface -C–SO$_3$H groups [42–44]. Thus, the XPS data indicate that the CDs are mainly composed of –C–SO$_3$H, C–S, C–O, and C═C chemical bonds, in accordance with

FTIR analysis.

3.2. Optical properties

Ultraviolet-visible (UV–Vis) absorption and photoluminescence (PL) spectra were recorded to evaluate the optical characteristics of the samples. As shown in Fig. 2a, the UV–Vis absorption spectra of 1,3-dihydroxynaphthalene (precursor) exhibited typical peaks at 284 and 332 nm due to π–π* and n–π* transition, respectively. Interestingly, the optical absorption band of aqueous O-CDs solution (DI water, neutral pH, 300 μg/mL) was bathochromically shifted to 510 nm owing to the π–π* transition of the conjugated carbogenic core, with continuous broad absorption band ranging from NIR to visible radiation. The O-CDs sample, dispersed in 70% ethanol, was excited at various excitation wavelengths, and the resultant PL emission spectra were recorded as shown in Figure S3a & S3b (ESI†). The PL spectra of O-CDs revealed excitation-dependent polychromatic emissions in the range of 540–640 nm, with the dual emission maxima at 540 and 580 nm, corresponding to yellow and orange emission at the excitation of 490 nm. Moreover, the as-synthesized O-CDs exhibited high aqueous dispersibility, making them a suitable agent for bio-application. Likewise, the O-CDs sample dispersed in water exhibited similar excitation-dependent polychromatic emissions in the range of 540–640 nm, with the dual emission maxima at 540 and 580 nm, as shown in Fig. 2b & Fig. 2c. Figure S3c (ESI†) & Fig. 2d display the excitation and emission contour profiles of O-CDs in ethanol and water, respectively. It is to be noted that in both the solvents, O-CDs exhibited maximum emission center in the yellow-orange region. O-CDs with photostable fluorescence and good intercellular distribution inspired us to inspect cellular imaging studies under fluorescence microscopy. Figure S3d (ESI†) shows the fluorescence microscopy images of cells treated with O-CDs (24 h
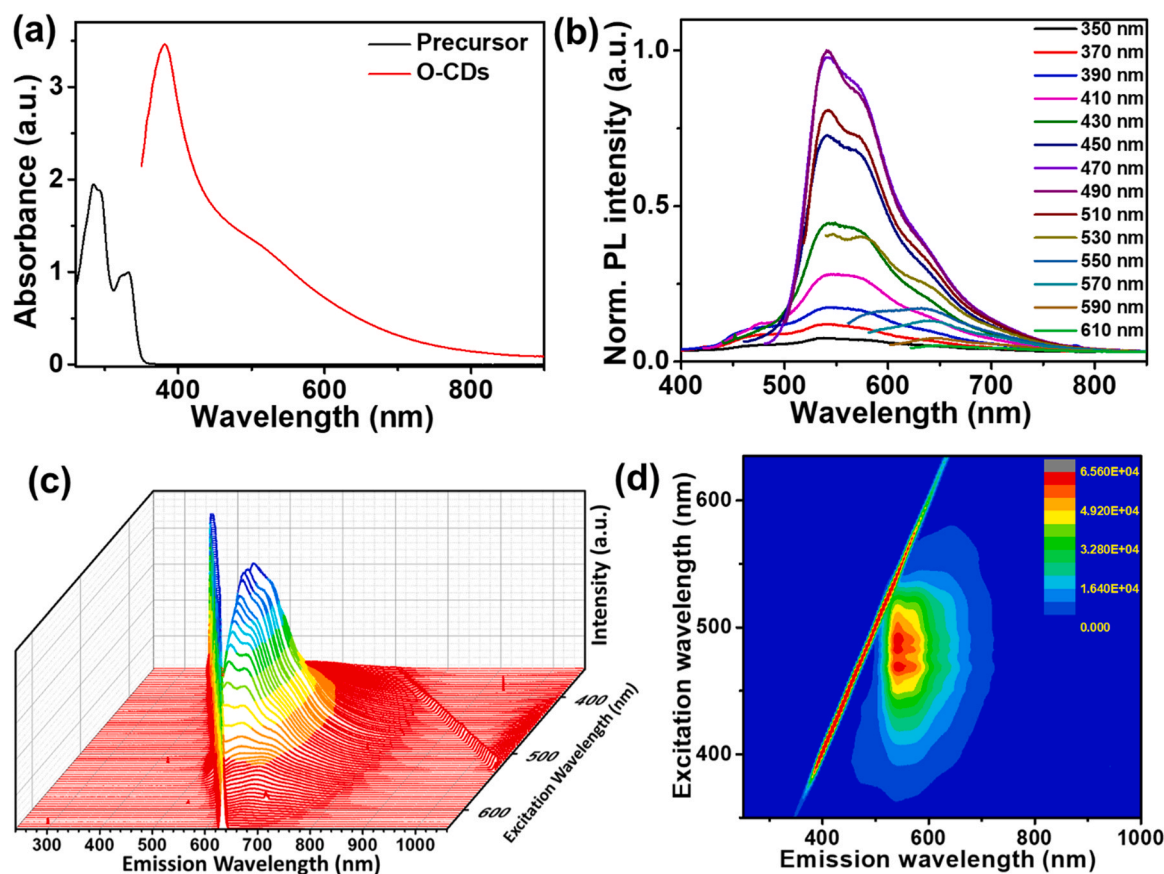

Fig. 2. (a) UV–Vis absorption spectra of precursor (black line) and O-CDs (red line); (b) PL emission spectra of O-CDs at various excitation wavelengths; (c) excitation-dependent PL emission spectra of O-CDs; (d) excitation and emission contour profile of O-CDs.

incubation) under bright fields, yellow/red channels, and merged images.

3.3. NIR-responsive photothermal properties

It is reasonable to consider O-CDs as a potential NIR-triggered photothermal agent due to its broad UV–Vis absorption spectra composed of continuous energy bands and the presence of an extended π-conjugated carbon framework [3,31,34]. The photothermal conversion performance of the aqueous O-CDs solution was assessed under the irradiation of NIR-light (808 nm). DI water was utilized as a control throughout the experiment. The procedure of the photothermal experiment and PCE calculation have been depicted in Section 2.2. An aqueous solution of O-CDs (200–400 μg/mL) was exposed to the constant irradiation of the NIR beam (808 nm, 10 mins) to determine the fluctuation in temperature as a function of irradiation time. Fig. 3a depicts the temperature rise pattern of aqueous O-CDs solution at different concentrations as a function of irradiation time for 10 min duration under the steady stimulation of NIR light (808 nm, 1 W/cm^2). It is to be noted that pure DI

water (control) didn't show a significant increase in temperature with a slight rise of 5 °C during irradiation for 10 min under continuous NIR irradiation. Interestingly, with a gradual increase in the O-CDs concentration from 200–400 μg/mL, the system exhibited an incremental rise in temperature. The aqueous O-CDs solution at the concentration of 200 and 400 μg/mL exhibited temperature rise up to 53 °C and 60.5 °C, respectively, at 1 W/cm^2 power density. The significant rise of temperature with an increase in O-CDs concentration probably originated due to higher absorption of NIR-light by the probe [3]. We also investigated the impact of NIR laser power density on photothermal by varying the NIR power density from 1 W/cm^2 to 1.5 W/cm^2. At higher power density, the aqueous O-CDs solution exhibited higher photothermal heat generation, resulting in elevated solution temperature. As shown in Fig. 3b, the aqueous O-CDs solution at the concentration of 200 and 400 μg/mL exhibited temperature rise up to 55.6 °C and 71.6 °C, respectively, at 1.5 W/cm^2 power density. Fig. 3c depicts the concentration-dependent temperature fluctuation (ΔT) over 10 min of NIR treatment at NIR power density of 1 W/cm^2 and 1.5 W/cm^2. It's obvious to note that the temperature deviation (ΔT) at higher laser
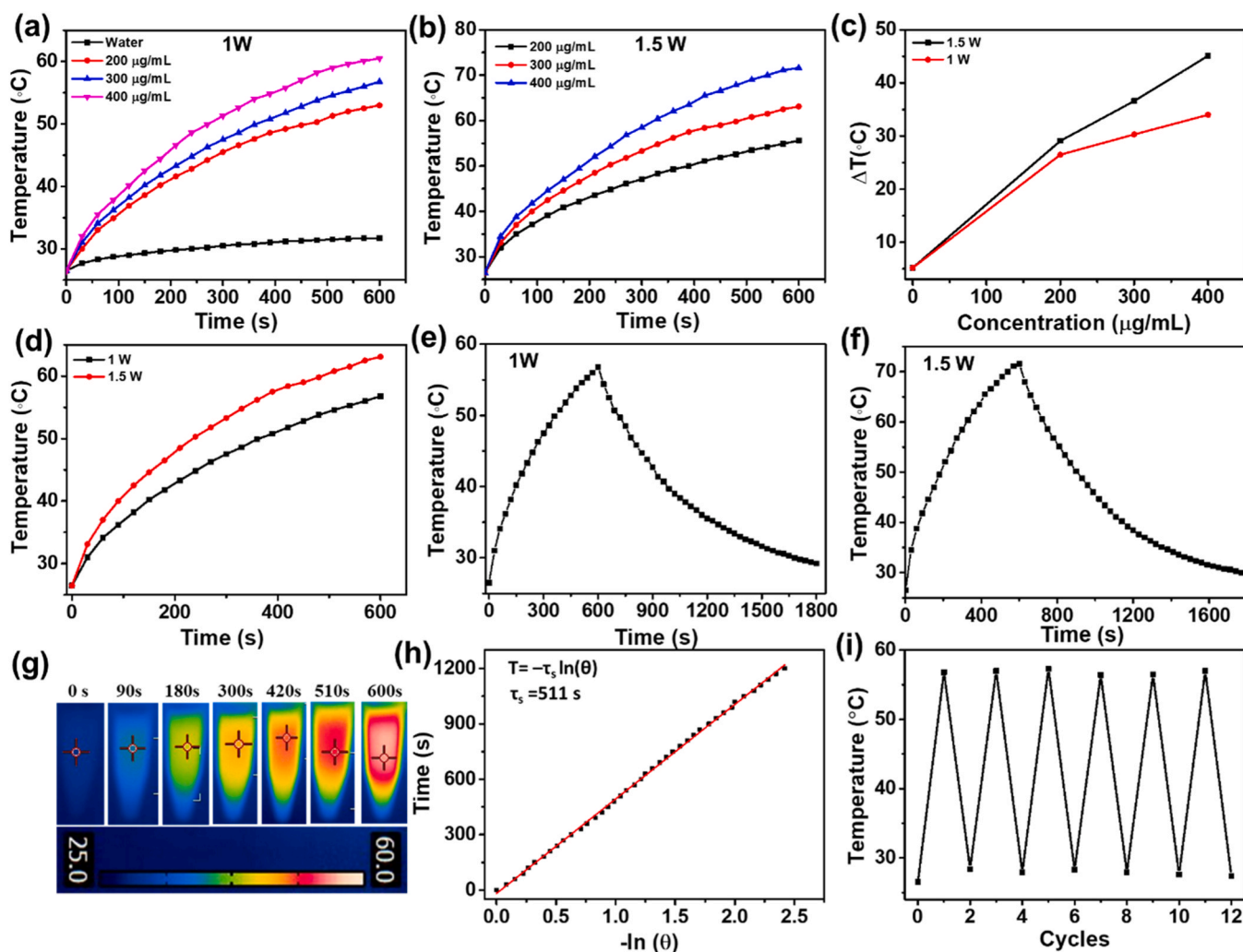
Fig. 3. Photothermal transformation characteristics of O-CDs. (a) Temperature elevation profile of aqueous O-CDs solutions (200–400 μg/mL) during continuous irradiation of NIR light (808 nm, 1 W/cm^2) for 600 s; (b) Temperature elevation profile of aqueous O-CDs solutions (200–400 μg/mL) during continuous irradiation of NIR light (808 nm, 1.5 W/cm^2) for 600 s; (c) Concentration-dependent temperature fluctuation (ΔT) over 10 min of NIR treatment at NIR power density of 1 W/cm^2 and 1.5 W/cm^2; (d) Temperature rise pattern of aqueous O-CDs solution (300 μg/mL) under NIR light at different power density (1 W/cm^2 and 1.5 W/cm^2); (e & f) temperature rise during NIR treatment and subsequent cooling profile after irradiation was stopped for O-CDs solutions (300 μg/mL, 1 W/cm^2 vs 300 μg/mL, 1.5 W/cm^2); (g) digital photographic thermal images of O-CDs solution (300 μg/mL) captured at various progressive time intervals.; (h) the linear plot of negative natural logarithm of the temperature driving force as a function of cooling time; (i) photothermal conversion stability of aqueous O-CDs solution (300 μg/mL) across six cycles of NIR-light on/off.

power intensity is more due to better absorption of light by the system. Fig. 3**d** depicts the temperature rise pattern of aqueous O-CDs solution (300 μg/mL) as a function of irradiation time for 10 min duration under the steady stimulation of NIR light at different power densities (1 W/cm^2 and 1.5 W/cm^2). The photothermal conversion efficiency was evaluated by recording the temperature variation of aqueous O-CDs solution (300 μg/mL) as a function of NIR-irradiation time under constant laser exposure (808 nm, 1 W/cm^2, 10 min). Fig. 3**e** depicts the temperature elevation pattern of aqueous O-CDs solution (300 μg/mL) during the NIR-irradiation at 1 W/cm^2 power density for 10 min and subsequent temperature fall due to normal cooling after turning the laser off. Fig. 3**f** shows a similar temperature elevation and subsequent temperature decline pattern under the same conditions but at different concentrations of O-CDs solution (400 μg/mL) and different NIR laser power densities (1.5 W/cm^2). Fig. 3**g** displays the digital photographic thermal images of O-CDs solution (300 μg/mL) captured at various progressive time intervals amid constant NIR irradiation, which demonstrate an excellent trend of photo-energy transformation into thermal energy. Fig. 3**h** is derived according to the data obtained from Fig. 3**e**, which depicts the linear plot of the negative natural logarithm of the temperature driving force as a function of cooling time. The system's heat transfer time constant (τ_S) was estimated to be 511 s. The experimental section described the measurement of PCE in detail, and it was found to be 58%. Moreover, the photothermal conversion stability of aqueous O-CDs solution (300 μg/mL) has been investigated, as shown in Fig. 3i, which shows exhibited good stability across six cycles of NIR-light on/off. Therefore, the above experimental results reveal that O-CDs can efficiently convert NIR beam energy into thermal energy, which could be an appropriate agent for the photothermal killing of cancer cells.

In recent years, there has been ongoing demand for designing CDs-based NIR-responsive photothermal agents with high PCE for photothermal therapy. For this purpose, researchers have deliberately explored diverse scopes by selecting proper CD precursors to synthesize polycyclic aromatic CDs with extended π-conjugation for better NIR absorption. Certain reports, which have been listed in Table 1, were able to design successful NIR-responsive CDs with extended π-conjugation and high PCE by judicious selection of proper precursors.

3.4. In vitro hyperthermia-induced anticancer activity

Owing to the outstanding photothermal properties of O-CDs, we inspected their invitro anticancer activity on cancerous cell lines. NIR-light-induced photothermal anticancer efficacy of O-CDs was evaluated against HepG2 as a model cancer cell line. As shown in Fig. 4**a**, we investigated *in vitro* cytotoxicity of O-CDs at different concentrations

Table 1
Literature survey on various precursor-derived CDs utilized as photothermal agents for therapeutic application.

| CDs precursor	Synthesis method	PL emission (nm)	Laser (nm)	PCE (%)	Application	Reference
citric acid and Urea and polydopamine	Hydrothermal	Green (520)	808	26.5	Photothermal anticancer	[45]
Hypocrella bambusae	Hydrothermal	Red (610)	635	27.6	Photodynamic/photothermal therapy of cancer	[26]
Watermelon juice	Hydrothermal	Blue (450)	808	30.6	Optical imaging and photothermal therapy	[28]
Polydopamine and folic acid	Hydrothermal	Blue (485)	808	32.1	photothermal therapy of prostate cancer cells	[46]
1,3,5-Trihydroxybenzene	Thermal heating	Yellow (550)	808	32.6	Bioimaging and photothermal bactericidal activity	[47]
Dopamine hydrochloride	Hydrothermal	Blue (450)	808	35	Photothermal cancer therapy	[48]
Ethylenediaminetetraacetic acid monosodium ferric salt	Pyrolysis	NA	808	35.1	Photothermal antibacterial therapy and wound healing	[49]
Polythiophene benzoic acid	Hydrothermal	Red (640)	635	36.2	Photodynamic/ photothermal therapy	[50]
zinc tetraphenylporphyrin	Hydrothermal	Red (630)	660	37	Photothermal Therapy and Photodynamic Therapy of Cancer	[51]
Nitropyrene and Polyethylenimine	Hydrothermal	Blue (475)	808	38.3	photothermal cancer therapy	[34]
Polythiophene phenylpropionic acid	Hydrothermal	Red (640)	671	38.5	Imaging and photothermal therapy	[27]
Cyanine dye and PEG800	Solvothermal	NIR (820)	808	38.7	Imaging and photothermal cancer therapy	[52]
Alcea extract and CuSO$_4$	Hydrothermal	Blue (460)	808	39.3	Cancer Photothermal Therapy	[53]
citric acid and dicyandiamide	Hydrothermal	Blue (450)	808	41.7	photothermal therapy of cancer cells	[54]
Citric acid and formamide	microwave	Red (640)	671	43.9	Photothermal cancer therapy	[55]
Citric acid and urea	Microwave-assisted hydrothermal	Blue (460)	655	54.3	Photothermal cancer therapy	[56]
Nitro-coronene derivative	Hydrothermal	Green	808	54.7	Photothermal Therapy of Cancer	[3]
Nitroperylene	Hydrothermal	Greenish yellow (538)	808	56.7	Photothermal Bactericidal activity	[31]
Polythiophene and diphenyl diselenide	Hydrothermal	Red (731)	635	58.2	photothermal therapy of cancer cells	[32]
Citric acid and urea	Solvothermal	NA	655	59.2	Photothermal tumor therapy	[57]
Trinitropyrene	Hydrothermal	Yellow (570)	635	73.5	photothermal/photodynamic cancer therapy	[30]
Nitrocoronene and BPEI	Microwave assisted hydrothermal	Blue (450)	808	77.8	photothermal eradication of multidrug-resistant bacteria	[29]
1,3-dihydroxynaphthalene	Open system thermal heating	Orange (580)	808	58	Photothermal killing of cancer cells	This work
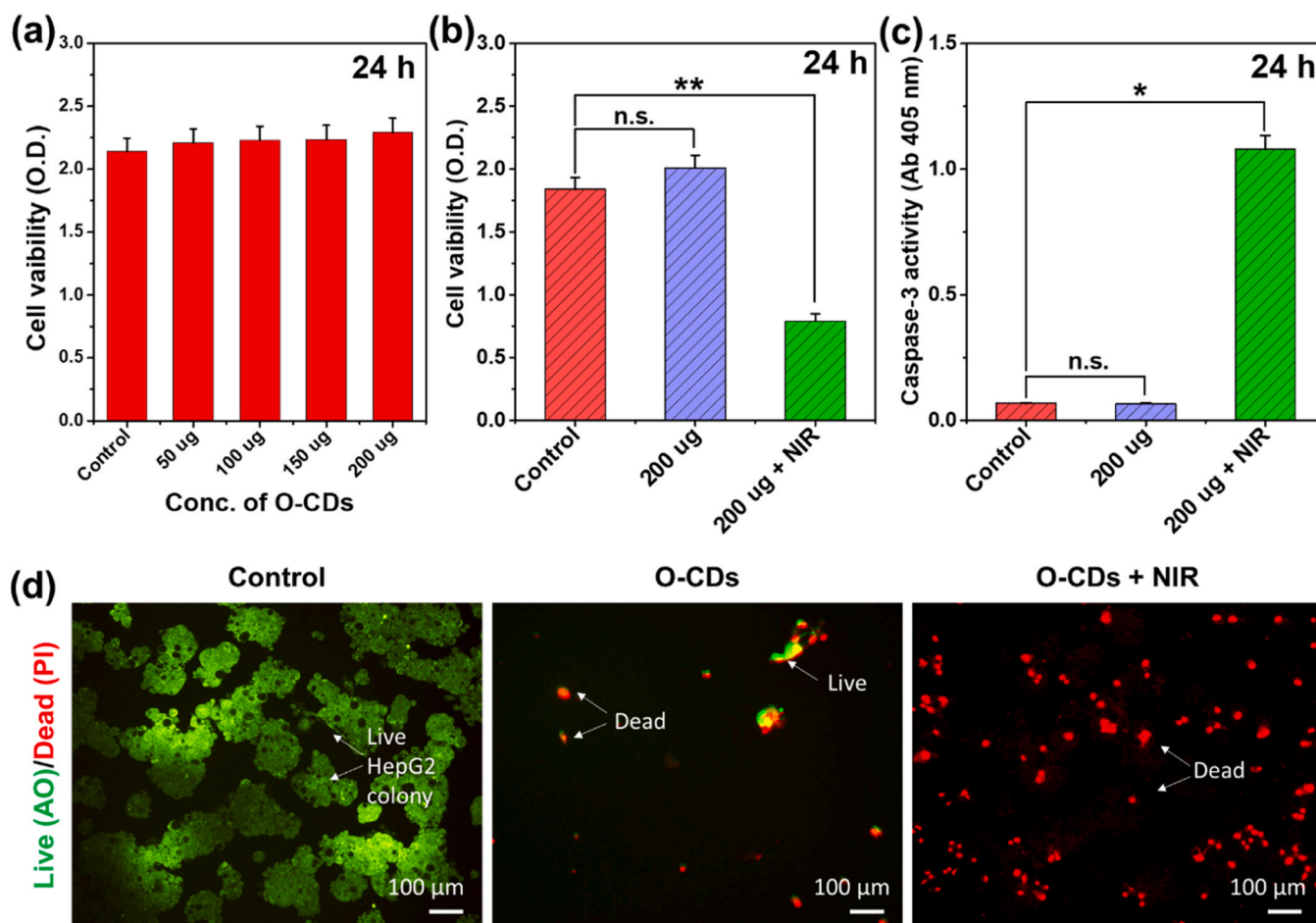
Fig. 4. (a) Cytotoxicity profile of O-CDs on HepG2 cells after 24 h of incubation.; (b) Cytotoxicity profile of O-CDs on HepG2 cells with and without NIR-treatment following 24 h of incubation; (c) detection of cytoplasmic apoptotic proteins (caspase-3 activity) with and without NIR-treatment following 24 h of incubation; (d) Live-dead essay indicating the impact of NIR-radiation and hyperthermia-induced cell death.

(50–200 μg mL^{-1}) on HepG2 cells. It is worth mentioning that HepG2 cells are very much viable at the concentration range of 50–200 μg mL^{-1} after 24 h of treatment. More interestingly, the cell even grows faster (~9.2%) at higher concentrations (200 μg mL-1), which indicates that the O-CDs samples had limited toxicity, probably due to low levels of oxidative stress in ambient conditions. Thus, we selected 200 μg mL^{-1} as a fixed dose concentration throughout the experiment. Subsequently, the effect of NIR-irradiation on cell viability was studied. Fig. 4**b** shows the cell viability data of HepG2 cells (with and without NIR treatment) for 24 h of culture. The survival ratio of cancerous HepG2 cells decreased abruptly, and only ~39.7% of cells were alive for the (O-CDs + NIR) treated sample as compared to the (O-CDs – NIR) treated sample. In other words, ~60.3% of cells died effectively due to the impact of NIR treatment. It is of utmost interest to inspect the upregulation activity of apoptosis-related proteins and gene expression, which is a phenomenal marker for oxidative stress-induced cellular damage. For *in vitro* detection of cytoplasmic apoptotic proteins, we investigated the upregulation of caspase-3 activity, as shown in Fig. 4**c**. The (O-CDs + NIR) treated HepG2 cells exhibited higher expression of cytoplasmic apoptotic caspase-3 proteins compared to the untreated groups. However, the (O-CDs – NIR) treated HepG2 cells didn't show significant expression of apoptotic Caspase-3 proteins. This experimental observation clearly reveals the impact of NIR-induced photothermal activation of the Caspase enzyme in HepG2 cells, a key indicator of programmed cell death (PCD) [58]. Moreover, the Live/Dead assay was further conducted to confirm the killing efficacy of O-CD + NIR treatment. As depicted in Fig. 4**(d)**, the control HepG2 cells displayed live cell colonies with no

noticeable dead cells. The O-CDs treated HepG2 cells showed some live and a few dead cells, whereas the NIR light irradiation significantly enhanced the number of dead cells, suggesting O-CD's efficacy for generating hyperthermia-induced cell death.

To get detailed insight into the mechanism of cell death, we studied the mRNA expression profile of various apoptotic and pro-apoptotic markers present in the cytoplasm, nucleus, and mitochondria, as shown in Fig. 5. As shown in Fig. 5**a**, the relative mRNA expression of nuclear anti-apoptotic proliferation marker *cyclin D1* decreased due to the presence of O-CDs (200 μg mL^{-1}), which further attenuated after NIR exposure. Similarly, the relative mRNA expression of mitochondrial anti-apoptotic marker *Bcl-2* was reduced owing to the O-CDs + NIR treatment, as shown in Fig. 5**b**. On the contrary, the 200-μg mL^{-1} dose of (O-CDs + NIR) significantly elevated the mRNA expression of mitochondrial pro-apoptotic marker *Bax* and cytoplasmic apoptotic marker *Caspase-3* as compared to the control group (Figs. 5**c and** 5**d**). The synergistic activation of this gene markers expression is intimately related to the apoptotic cell death in HepG2 [59–62]. Moreover, an in-depth analysis of protein expression was also performed in order to gain a thorough understanding of the cell death mechanism. The 200-μg mL^{-1} dose of (O-CDs + NIR) during 24 h of treatment significantly upregulated the expression of various cellular pro-apoptotic and anti-apoptotic proteins compared to the control group, as shown in Fig. 5**e**. The specified gene primers used in qRT-PCR analysis are listed in **Table S1 (ESI†)**. As shown in Fig. 5**(f-i),** the elevated expression of mitochondrial pro-apoptotic protein Bad, Bax, Bid, and Bim has been clearly revealed after (O-CDs + NIR) treatment as compared to the
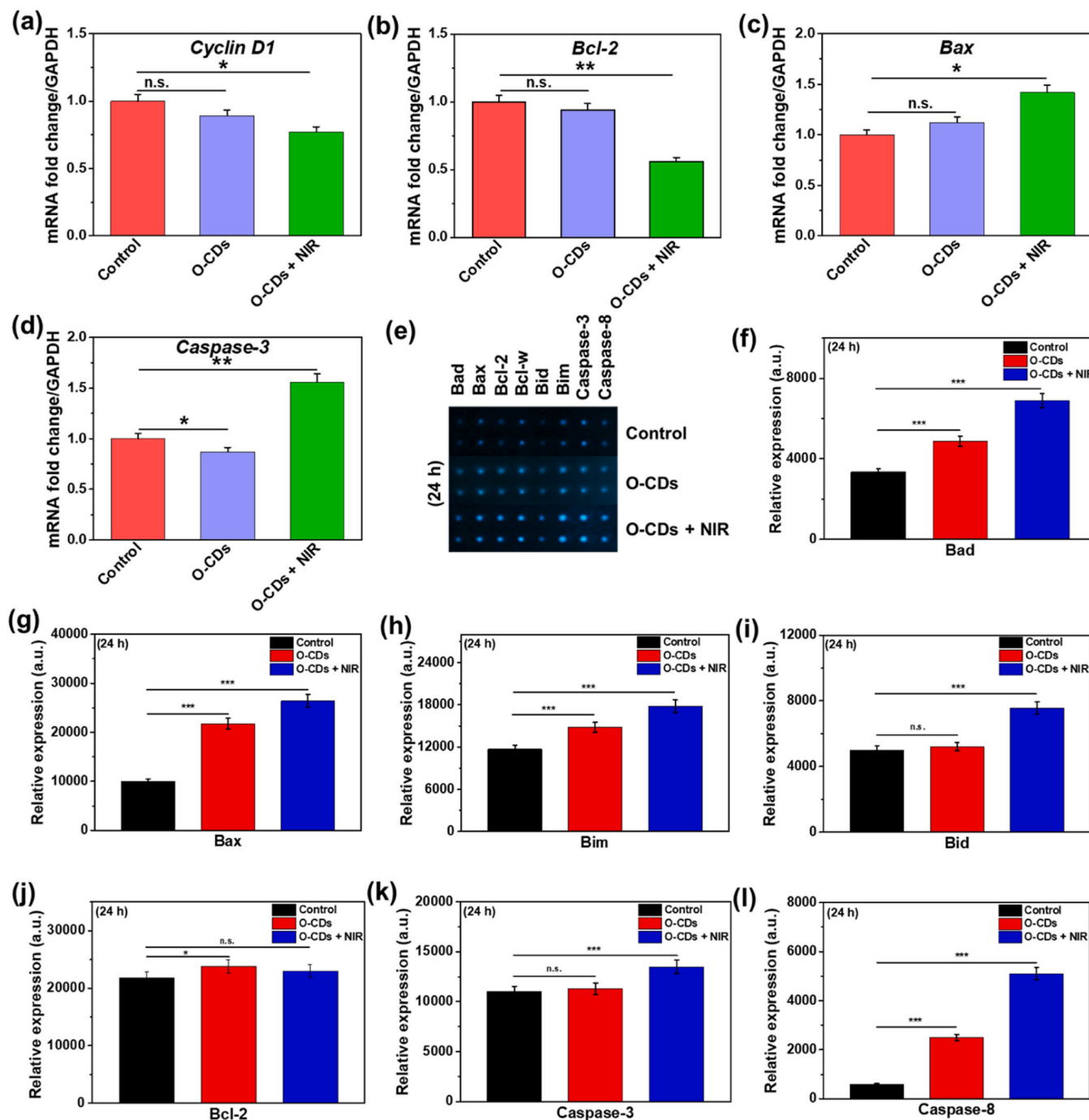
Fig. 5. Relative mRNA expression of (a) apoptosis-related nuclear gene marker *cyclin D1* (b-c) apoptosis-related mitochondrial gene marker *Bax* and *Bcl-2,* (d) apoptosis-related cytoplasmic gene marker *caspase-3* after 24 h of incubation in the presence of O-CDs (200-μg mL^{-1}) and NIR treatment.; quantification of apoptosis-related proteins (e) representative array membranes, (f-j) relative expression of apoptosis-related mitochondrial proteins (*Bad, Bax, Bim, Bid, & Bcl-2*), (k-l) relative expression of apoptosis-related cytoplasmic proteins (*Caspase-3 & Caspase-8*). Data are mean ± s.d. (n = 2); *p < 0.05, **p < 0.001, and ***p < 0.0001, analyzed by One-way ANOVA test.

control group, which suggests that mitochondria have direct involvement in oxidative-stress induced cellular damage [63–67]. The mitochondrial anti-apoptotic protein *Bcl-2,* which promotes cellular survival and inhibits the function of pro-apoptotic proteins, was not significantly expressed during 24 h of treatment compared to the control group (Fig. 5**j**), and the result is in accordance with the relative mRNA expression data of *Bcl-2* (Fig. 5**b**). Moreover, the expression of cytoplasmic proteins such as caspase-3 and caspase-8 were also elevated sharply upon (O-CDs + NIR) treatment as compared to the control group (Figure k&l). These caspase proteins are major initiators for apoptotic

fragmentation of DNA, cleavage of structural/cell cycle proteins, and are reliable markers for apoptosis-induced cell death [68,69]. Thus, activation of various mitochondrial as well as cytoplasmic pro-apoptotic/anti-apoptotic proteins suggests that hyperthermia and oxidative stress have a major impact on cell death during photothermal treatment.

From the experimental observation of cell viability as well as the relative expression of cellular genes and proteins in the presence and absence of NIR, it was clear that the radiation had a major impact on anticancer activity. To acquire a deeper understanding of the oxidative

stress-induced anticancer mechanism at the cellular level, we performed a fluorescence-based 2′, 7′-dichlorofluorescein diacetate (DCF-DA) assay on HepG2 cells [20]. A cell-membrane-permeable reagent called DCF-DA is frequently used to assess the generation of ROS within cells under stressful circumstances [70]. Typically, DCF-DA does not fluoresce; however, when cells are under oxidative stress, intracellular ROS may oxidize non-fluorescent DCF-DA to fluorescent DCF-DA [71]. Accordingly, the impact of O-CDs and NIR radiation on the production of intercellular ROS was assessed by monitoring the variation of fluorescence intensity. As shown in Fig. 6a, the intercellular fluorescence intensity of DCF-DA didn't show significant changes during 48 h in the absence of any external stress (O-CDs and NIR-radiation). Moreover, the intercellular fluorescence of DCF-DA exhibited a slight increase in intensity after 48 h in the presence of O-CDs under dark conditions, suggesting that O-CDs trigger the induction of intercellular ROS at a minor amount. However, the intercellular fluorescence of DCF-DA displayed very strong intensity in the presence of (O-CDs + NIR radiation), which suggests that a huge amount of intercellular ROS was produced specifically due to NIR treatment. To further support the production of NIR-induced intercellular ROS, we conducted electron spin resonance (ESR) spectra in the presence and absence of NIR radiation [31]. It has been frequently demonstrated that external light stimulation causes CDs to generate a significant quantity of ROS. We obtained ESR spectra of aqueous O-CDs solution with (2,2,6,6-tetramethylpiperidin-1-yl) oxyl (TEMPO) as a trapping agent for singlet oxygen ($^1O_2$) radical to examine the NIR-responsive ROS production. As shown in Fig. 6b, the ESR spectra of the control and O-CDs sample, in dark conditions (absence of NIR light), did not exhibit any characteristic peaks for $^1O_2$ radical. On the contrary, the ESR spectra of the aqueous O-CDs sample in the presence of NIR radiation exhibited multiple sharp characteristic signals with an equal intensity ratio of 1:1:1, corresponding to $^1O_2$ radical.

Thus, from the above experimental observation, it was revealed that O-CDs have excellent photothermal effects, intercellular ROS generation ability under oxidative stress, and upregulation of apoptosis-related genes/proteins under NIR-irradiation. It is a well-known fact that hyperthermia induces the rupture of cell membranes, while intercellular ROS induces DNA damage. Thus, the key mechanism for anticancer activity was probably due to the hyperthermia effect in cooperation with elevated intercellular ROS generation. O-CDs with extended π-conjugation may also interact with DNA via electrostatic interactions and π–π stacking, which induce DNA damage and upregulation of apoptosis-related genes and proteins [72]. Therefore, based on the results, we have illustrated a probable mechanism of apoptosis in cancer cells as shown in Fig. 7.
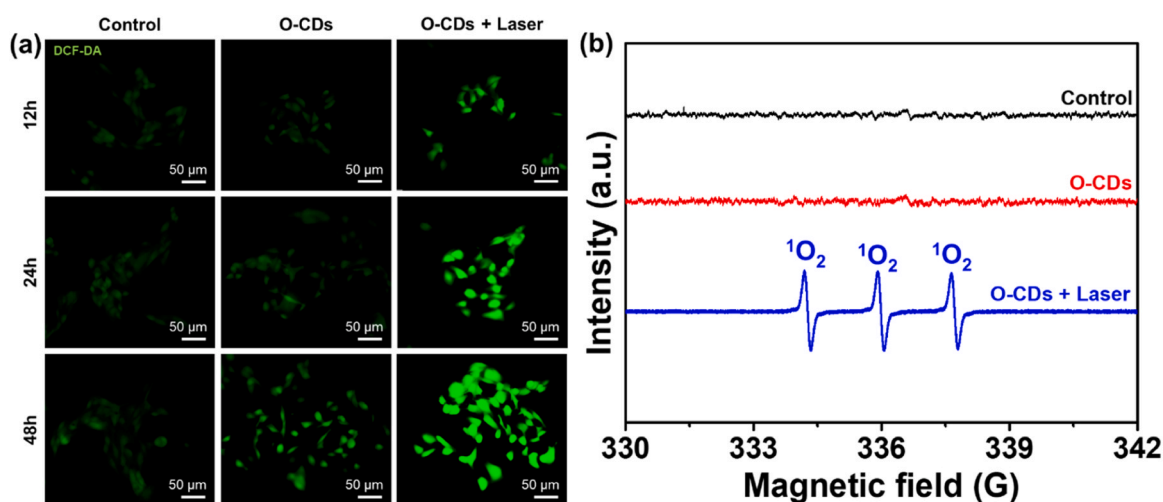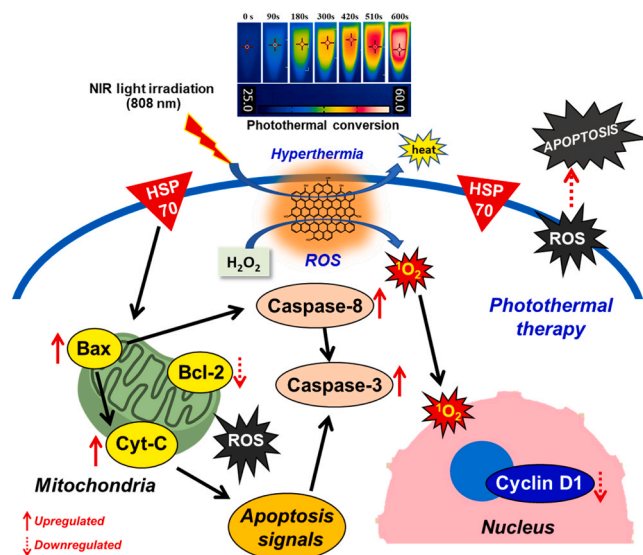

Fig. 7. Schematic illustration of the mechanism of apoptosis of cancer cells by the hyperthermia effect in cooperation with elevated intercellular ROS.

4. Conclusion

In summary, aqueous dispersible orange emissive CDs were produced rapidly by a simple wet chemistry-based technique with 1,3-dihydroxynaphthalene as a carbon precursor. As synthesized, O-CDs possessed broad absorption of NIR-radiation due to the π-conjugated structure. O-CDs exhibited outstanding NIR-harvesting properties with high PCE (~58%) and thus revealed impressive photothermal anticancer activity on HepG2 cells. Upon NIR (808 nm) treatment, O-CDs trigger hyperthermia and oxidative stress, which resulted in the upregulation of various mitochondrial as well as cytoplasmic apoptosis-related proteins and genes. The anticancer activity of O-CDs is likely due to the elevated reactive oxygen species amplification in cooperation with the hyperthermia effect. This study offers a potential substitute for imaging-guided, metal-free, carbon-based photothermal cancer therapy.

However, In the future, researchers will be more focused on exploring various suitable precursors for developing CDs with high PCE and longer wavelength responses in the NIR-II window, which is necessary for deep tissue penetration during *in-vivo* photothermal anticancer therapy.

Fig. 6. (a) DCFDA staining essay to determine oxidative-stress-induced intercellular ROS generation at various time intervals of incubation in the presence of O-CDs and NIR-radiation.; (b) ESR spectra of the aqueous O-CDs exhibiting characteristic signal of $^1O_2$ radicals in the presence of NIR light (808 nm, 1.5 W/cm^2).

CRediT authorship contribution statement

Ki-Taek Lim: Writing – review & editing, Visualization, Validation, Supervision, Resources, Project administration, Investigation, Funding acquisition, Conceptualization. **Sayan Deb Dutta:** Writing – review & editing, Writing – original draft, Visualization, Validation, Supervision, Software, Resources, Methodology, Investigation, Formal analysis, Data curation, Conceptualization. **Rumi Acharya:** Data curation, Methodology. **Jongsung Kim:** Writing – review & editing, Visualization, Validation, Supervision, Resources, Project administration, Investigation, Funding acquisition, Conceptualization. **Md Moniruzzaman:** Writing – review & editing, Writing – original draft, Visualization, Validation, Supervision, Software, Resources, Project administration, Methodology, Investigation, Funding acquisition, Formal analysis, Data curation, Conceptualization.

Declaration of Competing Interest

The authors declare that they have no known competing financial interests or personal relationships that could have appeared to influence the work reported in this paper.

Data Availability

Data will be made available on request.

Acknowledgments

Appendix A. Supporting information

Supplementary data associated with this article can be found in the online version at doi:10.1016/j.colsurfa.2024.134266.

References

[1] Y. Liu, P. Bhattarai, Z. Dai, X. Chen, Photothermal therapy and photoacoustic imaging: Via nanotheranostics in fighting cancer, Chem. Soc. Rev. 48 (2019) 2053–2108, https://doi.org/10.1039/c8cs00618k.

[2] H. Sun, Q. Zhang, J. Li, S. Peng, X. Wang, R. Cai, Near-infrared photoactivated nanomedicines for photothermal synergistic cancer therapy, Nano Today 37 (2021) 101073, https://doi.org/10.1016/j.nantod.2020.101073.

[3] S. Zhao, L. Yan, M. Cao, L. Huang, K. Yang, S. Wu, M. Lan, G. Niu, W. Zhang, Near-Infrared Light-Triggered Lysosome-Targetable Carbon Dots for Photothermal Therapy of Cancer, ACS Appl. Mater. Interfaces 13 (2021) 53610–53617, https://doi.org/10.1021/acsami.1c15926.

[4] W. Yin, L. Yan, J. Yu, G. Tian, L. Zhou, X. Zheng, X. Zhang, Y. Yong, J. Li, Z. Gu, Y. Zhao, High-throughput synthesis of single-layer MoS2 nanosheets as a near-infrared photothermal-triggered drug delivery for effective cancer therapy, ACS Nano 8 (2014) 6922–6933, https://doi.org/10.1021/nn501647j.

[5] Q. Chen, J. Wen, H. Li, Y. Xu, F. Liu, S. Sun, Recent advances in different modal imaging-guided photothermal therapy, Biomaterials 106 (2016) 144–166, https://doi.org/10.1016/j.biomaterials.2016.08.022.

[6] W. Bian, Y. Wang, Z. Pan, N. Chen, X. Li, W.L. Wong, X. Liu, Y. He, K. Zhang, Y. J. Lu, Review of Functionalized Nanomaterials for Photothermal Therapy of Cancers, ACS Appl. Nano Mater. 4 (2021) 11353–11385, https://doi.org/10.1021/acsanm.1c01903.

[7] C. Yu, L. Xu, Y. Zhang, P.S. Timashev, Y. Huang, X.J. Liang, Polymer-based nanomaterials for noninvasive cancer photothermal therapy, ACS Appl. Polym. Mater. 2 (2020) 4289–4305, https://doi.org/10.1021/acsapm.0c00704.

[8] H.S. Jung, P. Verwilst, A. Sharma, J. Shin, J.L. Sessler, J.S. Kim, Organic molecule-based photothermal agents: an expanding photothermal therapy universe, Chem. Soc. Rev. 47 (2018) 2280–2297, https://doi.org/10.1039/c7cs00522a.

[9] J. Chen, C. Ning, Z. Zhou, P. Yu, Y. Zhu, G. Tan, C. Mao, Nanomaterials as photothermal therapeutic agents, Prog. Mater. Sci. 99 (2019) 1–26, https://doi.org/10.1016/j.pmatsci.2018.07.005.

[10] X. Deng, Z. Shao, Y. Zhao, Solutions to the drawbacks of photothermal and photodynamic cancer therapy, Adv. Sci. 8 (2021) 1–16, https://doi.org/10.1002/advs.202002504.

[11] J.J. Hu, Y.J. Cheng, X.Z. Zhang, Recent advances in nanomaterials for enhanced photothermal therapy of tumors, Nanoscale 10 (2018) 22657–22672, https://doi.org/10.1039/c8nr07627h.

[12] K.J. Lagos, H.H. Buzzá, V.S. Bagnato, M.P. Romero, Carbon-based materials in photodynamic and photothermal therapies applied to tumor destruction, Int. J. Mol. Sci. 23 (2022), https://doi.org/10.3390/ijms23010022.

[13] Q. Jia, Z. Zhao, K. Liang, F. Nan, Y. Li, J. Wang, J. Ge, P. Wang, Recent advances and prospects of carbon dots in cancer nanotheranostics, Mater. Chem. Front. 4 (2020) 449–471, https://doi.org/10.1039/c9qm00667b.

[14] N. Sharma, G.S. Das, K. Yun, Green synthesis of multipurpose carbon quantum dots from red cabbage and estimation of their antioxidant potential and bio-labeling activity, Appl. Microbiol. Biotechnol. 104 (2020) 7187–7200, https://doi.org/10.1007/s00253-020-10726-5.

[15] N. Sharma, K. Yun, Dual sensing of tetracycline and L-Lysine using green synthesized carbon dots from Nigella sativa seeds, Dyes Pigments 182 (2020) 108640, https://doi.org/10.1016/j.dyepig.2020.108640.

[16] M. Moniruzzaman, B. Anantha Lakshmi, S. Kim, J. Kim, Preparation of shape-specific (trilateral and quadrilateral) carbon quantum dots towards multiple color emission, Nanoscale 12 (2020) 11947–11959, https://doi.org/10.1039/d0nr02225j.

[17] M. Moniruzzaman, J. Kim, Shape-engineered carbon quantum dots embedded on CdS-nanorods for enhanced visible light harvesting towards photocatalytic application, Appl. Surf. Sci. 552 (2021) 149372, https://doi.org/10.1016/j.apsusc.2021.149372.

[18] S.D. Dutta, J. Hexiu, J. Kim, S. Sarkar, J. Mondal, J.M. An, Y.K. Lee, M. Moniruzzaman, K.T. Lim, Two-photon excitable membrane targeting polyphenolic carbon dots for long-term imaging and pH-responsive chemotherapeutic drug delivery for synergistic tumor therapy, Biomater. Sci. 10 (2022) 1680–1696, https://doi.org/10.1039/d1bm01832a.

[19] S.D. Dutta, K. Ganguly, J. Hexiu, A. Randhawa, M. Moniruzzaman, K.T. Lim, A 3D bioprinted nanoengineered hydrogel with photoactivated drug delivery for tumor apoptosis and simultaneous bone regeneration via macrophage immunomodulation, 2300096, Macromol. Biosci. (2023) 1–15, https://doi.org/10.1002/mabi.202300096.

[20] M. Moniruzzaman, S.D. Dutta, J. Hexiu, K. Ganguly, K.-T. Lim, J. Kim, Polyphenol derived bioactive carbon quantum dot-incorporated multifunctional hydrogels as an oxidative stress attenuator for antiaging and in vivo wound-healing applications, Biomater. Sci. (2022), https://doi.org/10.1039/d2bm00424k.

[21] M. Moniruzzaman, J. Kim, Synthesis and post-synthesis strategies for polychromatic carbon dots toward unique and tunable multicolor photoluminescence and associated emission mechanism, Nanoscale 15 (2023) 13858–13885, https://doi.org/10.1039/d3nr02367b.

[22] G. Chellasamy, S.K. Arumugasamy, S. Govindaraju, K. Yun, Green synthesized carbon quantum dots from maple tree leaves for biosensing of Cesium and electrocatalytic oxidation of glycerol, Chemosphere 287 (2022) 131915, https://doi.org/10.1016/j.chemosphere.2021.131915.

[23] Y. Poojitha, G. Chellasamy, S. Govindaraju, K. Yun, Functionalized carbon quantum dots derived from zelkova serrata plant leaves for the detection of normetanephrine in geriatric plasma samples and ros-induced antibacterial applications using a plausible mechanistic approach, Biochip J. (2024), https://doi.org/10.1007/s13206-023-00136-w.

[24] S.K. Arumugasamy, S. Govindaraju, K. Yun, Electrochemical sensor for detecting dopamine using graphene quantum dots incorporated with multiwall carbon nanotubes, Appl. Surf. Sci. 508 (2020) 145294, https://doi.org/10.1016/j.apsusc.2020.145294.

[25] B. Li, S. Zhao, L. Huang, Q. Wang, J. Xiao, M. Lan, Recent advances and prospects of carbon dots in phototherapy, Chem. Eng. J. 408 (2021) 127245, https://doi.org/10.1016/j.cej.2020.127245.

[26] Q. Jia, X. Zheng, J. Ge, W. Liu, H. Ren, S. Chen, Y. Wen, H. Zhang, J. Wu, P. Wang, Synthesis of carbon dots from Hypocrella bambusae for bimodel fluorescence/photoacoustic imaging-guided synergistic photodynamic/photothermal therapy of cancer, J. Colloid Interface Sci. 526 (2018) 302–311, https://doi.org/10.1016/j.jcis.2018.05.005.

[27] J. Ge, Q. Jia, W. Liu, L. Guo, Q. Liu, M. Lan, H. Zhang, X. Meng, P. Wang, Red-emissive carbon dots for fluorescent, photoacoustic, and thermal theranostics in living mice, Adv. Mater. 27 (2015) 4169–4177, https://doi.org/10.1002/adma.201500323.

[28] Y. Li, G. Bai, S. Zeng, J. Hao, Theranostic carbon dots with innovative NIR-II emission for in vivo renal-excreted optical imaging and photothermal therapy, ACS Appl. Mater. Interfaces 11 (2019) 4737–4744, https://doi.org/10.1021/acsami.8b14877.

[29] B. Geng, Y. Li, J. Hu, Y. Chen, J. Huang, L. Shen, D. Pan, P. Li, Graphitic-N-doped graphene quantum dots for photothermal eradication of multidrug-resistant bacteria in the second near-infrared window, J. Mater. Chem. B 10 (2022) 3357–3365, https://doi.org/10.1039/d2tb00192f.

[30] S. Zhao, S. Wu, Q. Jia, L. Huang, M. Lan, P. Wang, W. Zhang, Lysosome-targetable carbon dots for highly efficient photothermal/photodynamic synergistic cancer therapy and photoacoustic/two-photon excited fluorescence imaging, Chem. Eng. J. 388 (2020) 124212, https://doi.org/10.1016/j.cej.2020.124212.

[31] M. Moniruzzaman, S.D. Dutta, K.T. Lim, J. Kim, Perylene-derived hydrophilic carbon dots with polychromatic emissions as superior bioimaging and NIR-responsive photothermal bactericidal agent, ACS Omega 7 (2022) 37388–37400, https://doi.org/10.1021/acsomega.2c04130.

[32] M. Lan, S. Zhao, Z. Zhang, L. Yan, L. Guo, G. Niu, J. Zhang, J. Zhao, H. Zhang, P. Wang, G. Zhu, C.S. Lee, W. Zhang, Two-photon-excited near-infrared emissive carbon dots as multifunctional agents for fluorescence imaging and photothermal therapy, Nano Res. 10 (2017) 3113–3123, https://doi.org/10.1007/s12274-017-1528-0.

[33] F. Wu, L. Chen, L. Yue, K. Wang, K. Cheng, J. Chen, X. Luo, T. Zhang, Small-molecule porphyrin-based organic nanoparticles with remarkable photothermal conversion efficiency for in vivo photoacoustic imaging and photothermal therapy, ACS Appl. Mater. Interfaces 11 (2019) 21408–21416, https://doi.org/10.1021/acsami.9b06866.

[34] B. Geng, D. Pan, L. Wang, F. Zheng, W. Shen, C. Zhang, X. Li, NIR-responsive carbon dots for efficient photothermal cancer therapy at low power densities, Carbon 134 (2018) 153–162, https://doi.org/10.1016/j.carbon.2018.03.084.

[35] Z. Wang, F. Yuan, X. Li, Y. Li, H. Zhong, L. Fan, S. Yang, 53% efficient red emissive carbon quantum dots for high color rendering and stable warm white-light-emitting diodes, Adv. Mater. 29 (2017) 1–7, https://doi.org/10.1002/adma.201702910.

[36] F. Yuan, T. Yuan, L. Sui, Z. Wang, Z. Xi, Y. Li, X. Li, L. Fan, Z. Tan, A. Chen, M. Jin, S. Yang, Engineering triangular carbon quantum dots with unprecedented narrow bandwidth emission for multicolored LEDs, Nat. Commun. 9 (2018) 1–11, https://doi.org/10.1038/s41467-018-04635-5.

[37] Y. Han, L. Liccardo, E. Moretti, H. Zhao, A. Vomiero, Synthesis, optical properties and applications of red/near-infrared carbon dots, J. Mater. Chem. C. 10 (2022) 11827–11847, https://doi.org/10.1039/d2tc02044k.

[38] E. Fuente, J.A. Menéndez, M.A. Díez, D. Suárez, M.A. Montes-Morán, Infrared spectroscopy of carbon materials: A quantum chemical study of model compounds, J. Phys. Chem. B 107 (2003) 6350–6359, https://doi.org/10.1021/jp027482g.

[39] C.S. Estes, A.Y. Gerard, J.D. Godward, S.B. Hayes, S.H. Liles, J.L. Shelton, T. S. Stewart, R.I. Webster, H.F. Webster, Preparation of highly functionalized carbon nanoparticles using a one-step acid dehydration of glycerol, Carbon 142 (2019) 547–557, https://doi.org/10.1016/j.carbon.2018.10.074.

[40] S. Suganuma, K. Nakajima, M. Kitano, D. Yamaguchi, H. Kato, S. Hayashi, M. Hara, Hydrolysis of cellulose by amorphous carbon bearing SO3H, COOH, and OH groups, J. Am. Chem. Soc. 130 (2008) 12787–12793, https://doi.org/10.1021/ja803983h.

[41] G. Yang, X. Wan, Y. Su, X. Zeng, J. Tang, Acidophilic S-doped carbon quantum dots derived from cellulose fibers and their fluorescence sensing performance for metal ions in an extremely strong acid environment, J. Mater. Chem. A 4 (2016) 12841–12849, https://doi.org/10.1039/c6ta05943k.

[42] Y.P. Wu, S. Fang, Y. Jiang, R. Holze, Effects of doped sulfur on electrochemical performance of carbon anode, J. Power Sources 108 (2002) 245–249, https://doi.org/10.1016/S0378-7753(02)00013-7.

[43] Y. Li, J. Wang, X. Li, D. Geng, M.N. Banis, Y. Tang, D. Wang, R. Li, T.K. Sham, X. Sun, Discharge product morphology and increased charge performance of lithium-oxygen batteries with graphene nanosheet electrodes: The effect of sulphur doping, J. Mater. Chem. 22 (2012) 20170–20174, https://doi.org/10.1039/c2jm34718k.

[44] Y. Wang, D. Wang, M. Tan, B. Jiang, J. Zheng, N. Tsubaki, M. Wu, Monodispersed Hollow SO3H-Functionalized Carbon/Silica as Efficient Solid Acid Catalyst for Esterification of Oleic Acid, ACS Appl. Mater. Interfaces 7 (2015) 26767–26775, https://doi.org/10.1021/acsami.5b08797.

[45] Q. Shu, J. Liu, Q. Chang, C. Liu, H. Wang, Y. Xie, X. Deng, Enhanced Photothermal Performance by Carbon Dot-Chelated Polydopamine Nanoparticles, ACS Biomater. Sci. Eng. 7 (2021) 5497–5505, https://doi.org/10.1021/acsbiomaterials.1c01045.

[46] L.M.T. Phan, A.R. Gul, T.N. Le, M.W. Kim, S.K. Kailasa, K.T. Oh, T.J. Park, One-pot synthesis of carbon dots with intrinsic folic acid for synergistic imaging-guided photothermal therapy of prostate cancer cells, Biomater. Sci. 7 (2019) 5187–5196, https://doi.org/10.1039/c9bm01228a.

[47] M. Moniruzzaman, S. Deb Dutta, K.-T. Lim, J. Kim, Wet chemistry-based processing of tunable polychromatic carbon quantum dots for multicolor bioimaging and enhanced NIR-triggered photothermal bactericidal efficacy, Appl. Surf. Sci. 597 (2022) 153630, https://doi.org/10.1016/j.apsusc.2022.153630.

[48] Y. Li, X. Zhang, M. Zheng, S. Liu, Z. Xie, Dopamine carbon nanodots as effective photothermal agents for cancer therapy, RSC Adv. 6 (2016) 54087–54091, https://doi.org/10.1039/c6ra02932a.

[49] Y. Liu, B. Xu, M. Lu, S. Li, J. Guo, F. Chen, X. Xiong, Z. Yin, H. Liu, D. Zhou, Ultrasmall Fe-doped carbon dots nanozymes for photoenhanced antibacterial therapy and wound healing, Bioact. Mater. 12 (2022) 246–256, https://doi.org/10.1016/j.bioactmat.2021.10.023.

[50] J. Ge, Q. Jia, W. Liu, M. Lan, B. Zhou, L. Guo, H. Zhou, H. Zhang, Y. Wang, Y. Gu, X. Meng, P. Wang, Carbon Dots with Intrinsic Theranostic Properties for Bioimaging, Red-Light-Triggered Photodynamic/Photothermal Simultaneous Therapy In Vitro and In Vivo, Adv. Healthc. Mater. 5 (2016) 665–675, https://doi.org/10.1002/adhm.201500720.

[51] J. Yue, P. Miao, L. Li, R. Yan, W.F. Dong, Q. Mei, Injectable carbon dots-based hydrogel for combined photothermal therapy and photodynamic therapy of cancer, ACS Appl. Mater. Interfaces (2022), https://doi.org/10.1021/acsami.2c15428.

[52] M. Zheng, Y. Li, S. Liu, W. Wang, Z. Xie, X. Jing, One-pot to synthesize multifunctional copper-doped carbon dots for near infrared fluorescence imaging and photothermal cancer therapy, ACS Appl. Mater. Interfaces 8 (2016) 23533–23541, https://doi.org/10.1021/acsami.6b07453.

[53] M. Najaflu, M. Shahgolzari, F. Bani, A.Y. Khosroushahi, Green synthesis of near-infrared copper-doped carbon dots from alcea for cancer photothermal therapy, ACS Omega 7 (2022) 34573–34582, https://doi.org/10.1021/acsomega.2c04484.

[54] Y. Shen, X. Zhang, L. Liang, J. Yue, D. Huang, W. Xu, W. Shi, C. Liang, S. Xu, Mitochondria-targeting supra-carbon dots: enhanced photothermal therapy selective to cancer cells and their hyperthermia molecular actions, Carbon 156 (2020) 558–567, https://doi.org/10.1016/j.carbon.2019.09.079.

[55] S. Sun, L. Zhang, K. Jiang, A. Wu, H. Lin, Toward high-efficient red emissive carbon dots: facile preparation, unique properties, and applications as multifunctional theranostic agents, Chem. Mater. 28 (2016) 8659–8668, https://doi.org/10.1021/acs.chemmater.6b03695.

[56] F.A. Permatasari, H. Fukazawa, T. Ogi, F. Iskandar, K. Okuyama, Design of pyrrolic-N-rich carbon dots with absorption in the first near-infrared window for photothermal therapy, ACS Appl. Nano Mater. 1 (2018) 2368–2375, https://doi.org/10.1021/acsanm.8b00497.

[57] X. Bao, Y. Yuan, J. Chen, B. Zhang, D. Li, D. Zhou, P. Jing, G. Xu, Y. Wang, K. Holá, D. Shen, C. Wu, L. Song, C. Liu, R. Zbořil, S. Qu, In vivo theranostics with near-infrared-emitting carbon dots—highly efficient photothermal therapy based on passive targeting after intravenous administration, Light.: Sci. Appl. 7 (1) (2018) 11, https://doi.org/10.1038/s41377-018-0090-1.

[58] Y. Hu, L. Zhang, S. Chen, L. Hou, S. Zhao, Y. Huang, H. Liang, Multifunctional carbon dots with near-infrared absorption and emission for targeted delivery of anticancer drugs, tumor tissue imaging and chemo/photothermal synergistic therapy, Nanoscale Adv. 3 (2021) 6869–6875, https://doi.org/10.1039/d1na00595b.

[59] A. Ambrosone, L. Mattera, V. Marchesano, A. Quarta, A.S. Susha, A. Tino, A. L. Rogach, C. Tortiglione, Mechanisms underlying toxicity induced by CdTe quantum dots determined in an invertebrate model organism, Biomaterials 33 (2012) 1991–2000, https://doi.org/10.1016/j.biomaterials.2011.11.041.

[60] S. Ganesh, K. Venkatakrishnan, B. Tan, Quantum scale organic semiconductors for SERS detection of DNA methylation and gene expression, Nat. Commun. 11 (2020), https://doi.org/10.1038/s41467-020-14774-3.

[61] J. Noh, B. Kwon, E. Han, M. Park, W. Yang, W. Cho, W. Yoo, G. Khang, D. Lee, Amplification of oxidative stress by a dual stimuli-responsive hybrid drug enhances cancer cell death, Nat. Commun. 6 (2015), https://doi.org/10.1038/ncomms7907.

[62] Y. Shang, Q. Wang, B. Wu, Q. Zhao, J. Li, X. Huang, W. Chen, R. Gui, Platelet-Membrane-Camouflaged Black Phosphorus Quantum Dots Enhance Anticancer Effect Mediated by Apoptosis and Autophagy, ACS Appl. Mater. Interfaces 11 (2019) 28254–28266, https://doi.org/10.1021/acsami.9b04735.

[63] J. Ge, M. Lan, B. Zhou, W. Liu, L. Guo, H. Wang, Q. Jia, G. Niu, X. Huang, H. Zhou, X. Meng, P. Wang, C.S. Lee, W. Zhang, X. Han, A graphene quantum dot photodynamic therapy agent with high singlet oxygen generation, Nat. Commun. 5 (1) (2014) 8, https://doi.org/10.1038/ncomms5596.

[64] Y. Chong, Y. Ma, H. Shen, X. Tu, X. Zhou, J. Xu, J. Dai, S. Fan, Z. Zhang, The in vitro and in vivo toxicity of graphene quantum dots, Biomaterials 35 (2014) 5041–5048, https://doi.org/10.1016/j.biomaterials.2014.03.021.

[65] X. Ma, R. Hartmann, D. Jimenez De Aberasturi, F. Yang, S.J.H. Soenen, B. B. Manshian, J. Franz, D. Valdeperez, B. Pelaz, N. Feliu, N. Hampp, C. Riethmüller, H. Vieker, N. Frese, A. Gölzhäuser, M. Simonich, R.L. Tanguay, X.J. Liang, W. J. Parak, Colloidal Gold Nanoparticles Induce Changes in Cellular and Subcellular Morphology, ACS Nano 11 (2017) 7807–7820, https://doi.org/10.1021/acsnano.7b01760.

[66] C.F. Labuschagne, E.C. Cheung, J. Blagih, M.C. Domart, K.H. Vousden, Cell Clustering Promotes a Metabolic Switch that Supports Metastatic Colonization, Cell Metab. 30 (2019) 720–734.e5, https://doi.org/10.1016/j.cmet.2019.07.014.

[67] S.S. Sabharwal, P.T. Schumacker, Mitochondrial ROS in cancer: Initiators, amplifiers or an Achilles' heel? Nat. Rev. Cancer 14 (2014) 709–721, https://doi.org/10.1038/nrc3803.

[68] D. Zhang, D. Wen, R. Huang, H. Wang, X. Hu, D. Xing, Mitochondrial specific photodynamic therapy by rare-earth nanoparticles mediated near-infrared graphene quantum dots, Biomaterials 153 (2018) 14–26, https://doi.org/10.1016/j.biomaterials.2017.10.034.

[69] Z. Wang, F. Cai, X. Chen, M. Luo, L. Hu, Y. Lu, The Role of Mitochondria-Derived Reactive Oxygen Species in Hyperthermia-Induced Platelet Apoptosis, PLoS ONE 8 (2013) 1–14, https://doi.org/10.1371/journal.pone.0075044.

[70] H.K. Kim, Adenophora remotiflora protects human skin keratinocytes against UVB-induced photo-damage by regulating antioxidative activity and MMP-1 expression, Nutr. Res. Pract. 10 (2016) 371–376, https://doi.org/10.4162/nrp.2016.10.4.371.

[71] W.H. Chan, C.C. Wu, J.S. Yu, Curcumin inhibits UV irradiation-induced oxidative stress and apoptotic biochemical changes in human epidermoid carcinoma A431 cells, J. Cell. Biochem. 90 (2003) 327–338, https://doi.org/10.1002/jcb.10638.

[72] L. Qi, T. Pan, L. Ou, Z. Ye, C. Yu, B. Bao, Z. Wu, D. Cao, L. Dai, Biocompatible nucleus-targeted graphene quantum dots for selective killing of cancer cells via DNA damage, Commun. Biol. 4 (2021) 1–12, https://doi.org/10.1038/s42003-021-01713-1.